RSC Advances

Electrochemical synthesis of Fe oxide-based catalysts for the growth of nanocarbons

Journal:	*RSC Advances*
Manuscript ID:	RA-ART-09-2014-009803.R1
Article Type:	Paper
Date Submitted by the Author:	31-Oct-2014
Complete List of Authors:	Pérez Villar, Sofía; CIC Energigune, Carretero-Gonzalez, Javier; CIC Energigune,

RCS Advances

RSCPublishing

ARTICLE

Electrochemical synthesis of Fe oxide-based catalysts for the growth of nanocarbons

Sofía Pérez-Villar,* Javier Carretero-González

Received ooth January 2014,
Accepted ooth January 2014

DOI: 10.1039/xoxx00000x

www.rsc.org/

Pulsed electrodeposition technique has been used for the synthesis of iron–based compounds as catalytic precursor for the growth of carbon nanofilaments *via* chemical vapor deposition (CVD). Iron-based nanoparticles were electrodeposited on a three–dimensional and electron conducting Al–Mg alloy substrate. A systematic control of the chemical composition, size and density of the iron-based nanoparticles was achieved by varying the nature of the electrolytic bath and the plating conditions. Results show that the as-prepared iron deposits synthesized at room temperature ($FeCl_3$) and at 50 ºC ($FeCl_2$ and $Fe(NO_3)_3$) are catalytically active for the growth of different carbon nanostructures. The structure of the catalyst precursor as well as their chemical composition has a direct influence on the final carbon nanostructure. Nanocarbons produced by this route exhibit a more disordered microstructure and higher concentration of defects than other carbon nanostructures like nanotubes produced also by CVD. These filamentous nanocarbons could be of practical and fundamental interest as electrodes in batteries, supercapacitors, fuel cells and sensors.

Introduction

Nanocarbons, such as graphene, carbon nanotubes and other low-dimensional crystalline carbons are of fundamental and practical interest, offering the possibility to develop new types of both high surface area and high electrical conductivity materials for a wide range of technological applications[1]. Yet, the lack of homogeneous single walled carbon nanotube and graphene sheets becomes a major obstacle that hinders their broad application.

The chemical vapor deposition (CVD) of carbon on transition metal nanoparticles has been shown to produce highly graphitic phases in a variety of morphologies.[2] Fundamental properties, such as crystal structure and electronic conductivity in nanocarbons prepared by CVD are highly influenced by the size, crystal morphology and chemical composition of the metal nanoparticles used in the catalytic growth.[3] Thus, the tunning of the catalyst particle morphology and composition may provide an effective way for targeting desirable functional properties for low–dimension crystalline nanocarbons. Iron–based nanoparticles are one of the most frequently used growth catalysts for nanostructured carbons mainly because of the relatively low cost of iron precursors, good efficiency and their high catalytic activity.[4] Usually, these iron catalysts are prepared by different methods like impregnation of a substrate with an iron salt–containing solution, physical deposition leading catalytic thin films or by floating chemical vapor deposition using ferrocene as main carbon feedstock and catalyst.[5]

Electrochemical deposition is a straight–forward, scalable and inexpensive method to prepare catalytic nanoparticles for a site–selective growth of filamentous carbon. Moreover, by using electropulsed technique is possible tune both the pulse amplitude and width[6,7] of the voltage (potentiostatic) or current (galvanostatic) as well as the plating media controlling ultimately the crystal morphology and structure, composition, and textural properties of the deposited metal film.[8] These are advantages with respect to the continous deposition which nuclei growth homogeneity is difficult to obtain.

A few studies on iron oxide plating to produce magnetite (Fe_3O_4) and hematite (α-Fe_2O_3) phases on different substrates have been published. For example, hematite deposits were synthesized by thermal oxidation in air at 500 ºC after pulse electrodeposition and by using Fe^0 or γ-FeOOH as precursors [9-11]. Nevertheless, magnetite thin films[12-14] were synthesized in aqueous media by controlling the pH and temperature bath at 70 ºC.

In our study, we are able to prepare iron oxide phases without any additional anealing after its synthesis and in a non-aqueous media. In previous work, our group demonstrated[15] as a proof of concept that with the combination of pulsed electrodeposition and CVD led to the preparation of novel filamentous carbon exhibiting high gravimetric edge surface and high density of reaction sites comparable to graphene. The purpose of this work is, first, to control the morphology and chemical composition of distinct iron-based particles at nano- and micro-scale by adjusting the plating media, temperature and iron salts by pulsed electrodeposition. Secondly, to study the impact of the the morphological, size, textural of different iron-based nanoparticles prepared by electrodeposition on the final carbon nanostructures obtained by CVD.

Results and discussion

The reduction potential of the oxidized iron species (Fe^{3+}, Fe^{2+}) to metallic iron was determined by linear sweep voltammetry (LSV). Note that all the potentials are referring to Ag/AgCl. Figure 1 shows the LSV plot recorded between 0.0 V to -2.5 V for the three Fe salts in formamide (FA) at room temperature (RT). The onset point of the cathodic current starts at -1.1 V, -1.3 V and -1.9 V for $FeCl_3.6H_2O$, $FeCl_2$, and $Fe(NO_3)_3.9H_2O$, respectively. For the three systems, a broad reduction peak is observed around -1.5 V. This is related to the electrochemical process Fe (II) + 2e → Fe (0) for anhydrous $FeCl_2$ salt and Fe (III) + e → Fe (II) + 2e → Fe(0) for $FeCl_3$. For the nitrate, a reduction of NO_3^- and local change in pH can also be considered. The current is decreasing abruptly with potential most probably due to solvent decomposition. From these results, the deposition potential for the pulsed electrodeposition (PED) experiments was set at -1.5 V. LSV plot at 50ºC and 100 ºC is reported in Figure 1S.

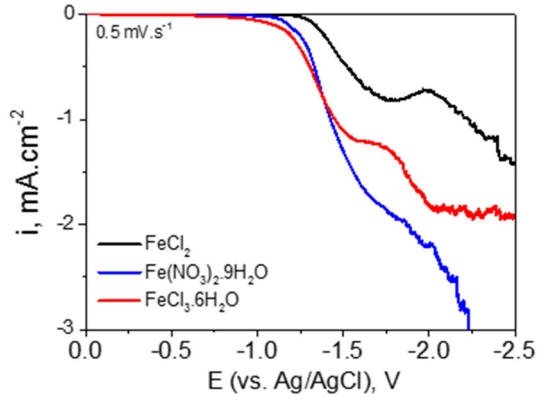

Fig. 1 Linear sweep voltammetry for the different iron-based baths at room temperature. The cell configuration was the following: working electrode: Al–Mg mesh; counter electrode: platinum foil; and reference electrode: Ag/AgCl.

At this potential, diverse and well-adhering films of iron-based nanoparticles were prepared by PED. Figure 2 shows the potentiostatic current–time transients for $FeCl_2$ at RT, 50 ºC and 100 ºC. The three experiments present a gradually increase in current density with temperature: 1.0, 2.0 and 4.0 mA, respectively. During the time–off (T_{off}), ions migrate to the depleted areas in the bath and desorption of deposited ions (see inset in Figure 2). On the other hand, while the time–on (T_{on}) occurs, more evenly distributed ions are available for the formation of the first nuclei and growth of the existing crystals[16]. After the formation of the initial nuclei of a crystal grain the number of grains per unit area increased with time. Finally, the electrodeposited material continues growing on the surface of the substrate. Along with the inset in Fig. 2, we observe that the current increased during the T_{on} with the bath temperature. This fact means that the kinetic diffusion is enhanced with temperature and consequently the mass transport diffusion leading a higher population density of particles at 100 ºC. [17] The jagged profile evidenced at 100 ºC (Figure 2a) is probably due to the high convective flow of solvent produced in a static media (no stirring). Potentiostatic current-time transients at 50ºC and 100 ºC are reported in Figure 2S. The maximum current intensity reached at different temperatures were 0.05, 1.49, and 2.80 mA for $FeCl_2$, 0.32, 1.52, and 17.5 mA for $FeCl_3.6H_2O$, and 0.04, 0.23, 6.56 mA for $Fe(NO_3)_3.9H_2O$.
Figure 3 presents SEM images of the electrochemically deposited iron–based material at different temperatures (RT, 50, 100 ºC). In general, the iron–based deposits exhibited a homogeneous dispersion all along the 3D substrate along with a broad Fe based aggregates–particles size distribution (between 0.1 to 20 µm). Furthermore, deposits have shown an increase in the number of nuclei with the increase of temperature.

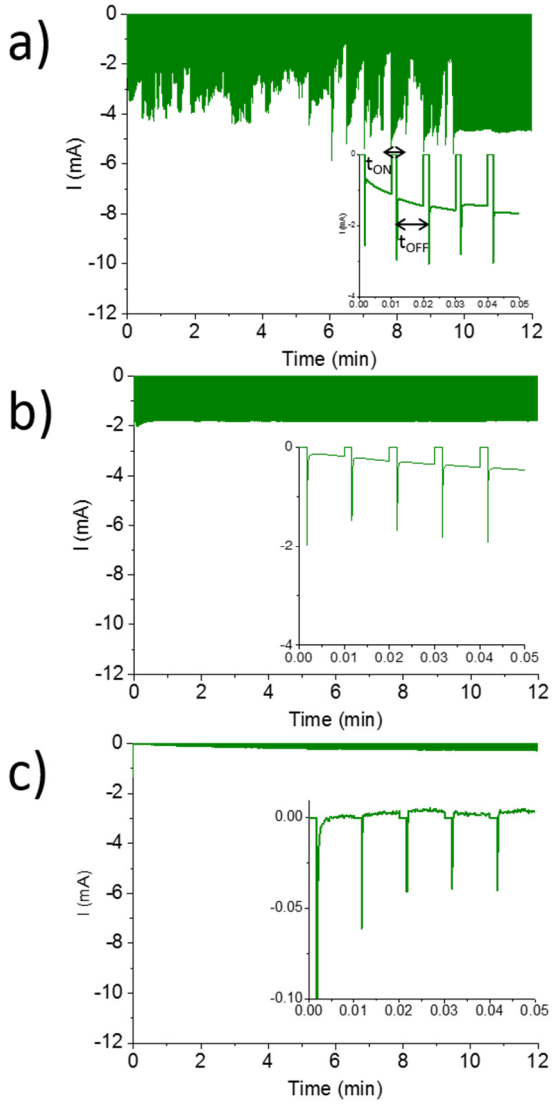

Fig. 2 Potentiostatic current-time transients for $FeCl_2$ at 100 ºC (a), 50 ºC (b) and RT (c) Inset: description of the typical pulse-potential waveform with cathodic pulses at the three different temperatures.

For the $FeCl_2$-based bath, Figure 3a shows spherical aggregates of around 10 µm with a crystal size between 2–5 µm. For instance, at 50 ºC and at 100 ºC (Fig. 3a), a shell covering the aggregates was observed. For the $FeCl_3$-based bath, Figure 3b shows the formation of a thin film with segregated particles of ~ 1 µm size at RT. When temperature increased, nanometric, primary particles would be found in round and isolated agglomerates of ~ 2µm. Finally, a compact surface covered by nanoparticles was formed at 100 ºC. Similar behaviour was observed in Figure 3c ($Fe(NO_3)_3$-based bath), where the only difference was a change in the size (10 µm) and morphology of

the deposits formed at 50 ºC. These results are in good agreement with those shown in Figure 2.

Because of the low amount of material produced by PED on the surface of the substrate, Raman spectroscopy is a suitable and powerful characterization technique to identify the vibrational modes of the distinct iron (oxide) phases. In Fig. 4 is represented the Raman spectra of the samples prepared by PED by using different iron precursors at different temperatures (RT, 50 °C, 100 ºC).

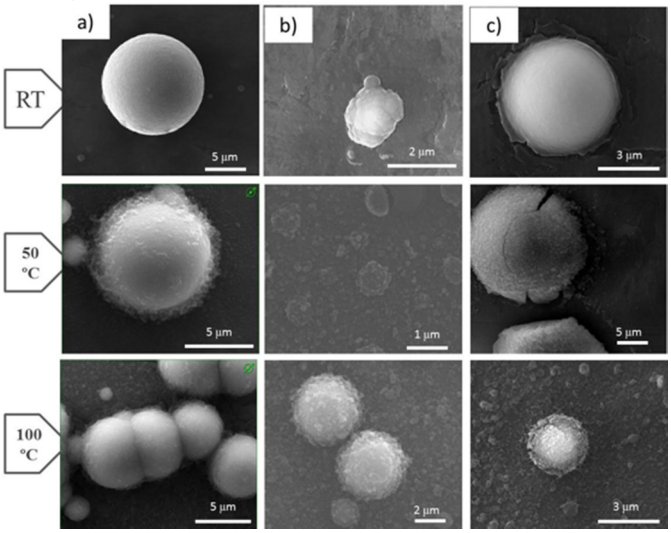

Fig. 3 SEM images of iron-based films prepared from (a) anhydrous $FeCl_2$, (b) $FeCl_3.6H_2O$ (c) $Fe(NO_3)_3.9H_2O$ at different temperatures.

As a summary, band positions and symetry of magnetite (Fe_3O_4) and hematite (α-Fe_2O_3) are also reported in Table 1.

Table 1 Wavenumber and symetry assingments for hematite and magnetite according to the references.

Hematite (α-Fe_2O_3)			Magnetite (Fe_3O_4)		
Raman shift (cm^{-1})		Symetry	Raman shift (cm^{-1})		Symetry
Reference 9-11	Our study		Reference 12-14	Our study	
225-229	217	A_{1g}	300-310	307	T_{2g}
245-249		E_g	530-554	530	T_{2g}
292-295	275	E_g	660-670	660	A_{1g}
299-302		E_g			
410-414	385	E_g			
497-500		A_{1g}			
611-615	588	E_g			

At room temperature, the Raman spectrum of the sample synthesized by using a $FeCl_2$–based bath (Fig. 4a) exhibited the main spectral signatures corresponding to the hematite phase (α-Fe_2O_3) being the most intense band assigned to the E_g vibrational mode (295 cm^{-1})[18,19]. The material prepared from the plating bath containing the hydrated Fe salts (Fig. 4b and 4 c) did not shown any characteristic bands at RT. The fluorescence was most probably due to the presence of a thin film of particles formed on the surface of the Raman–inactive substrate. No other impurities or iron phases were observed. At temperatures up to 100 ºC, a pronounced band at 660 cm^{-1} appeared in the three systems (Fig. 4 a-c). This peak was assigned to A_{1g} mode[20] and it corresponds to the magnetite phase (Fe_3O_4). Thus, the synthesis of this phase might be favored at higher temperature in agreement to the literature.[12] For the hydrated salt-based ($FeCl_3$ and $Fe(NO_3)_3$, both iron oxide phases, α-Fe_2O_3 and Fe_3O_4, coexisted at 100 ºC. Maybe a second layer of hematite was produced on magnetite particles. Moreover, we would like to point out that for the $Fe(NO_3)_3$ hydrated bath (Fig. 4c), the electrochemical synthesis of iron oxides compounds yields more amorphous phases as it was evidenced by the higher signal–to–noise ratio in the spectrum than their counterparts.

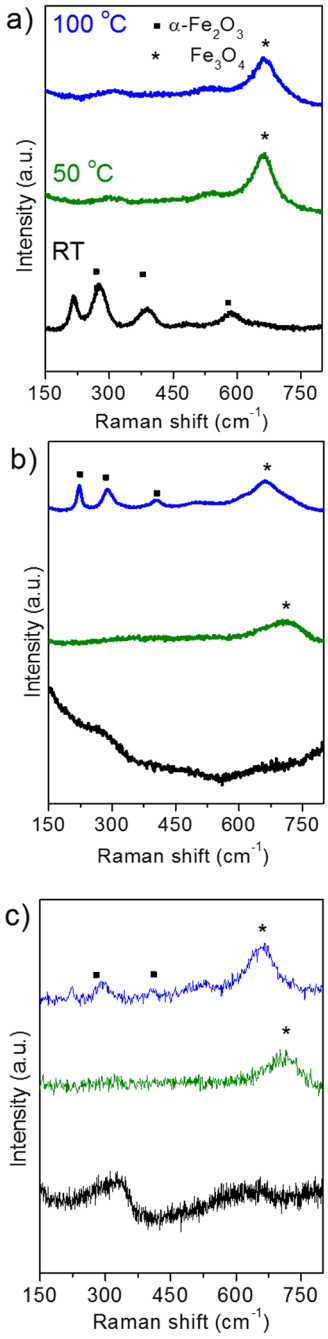

Fig. 4 Raman spectra of the iron-based deposits produced by PED from (a) anhydrous $FeCl_2$, (b) $FeCl_3.6H_2O$ (c) $Fe(NO_3)_3.9H_2O$ at different temperatures.

Our results revealed that complex interfacial reactions could produced different iron phases such as Fe clusters, Fe_2O_3, Fe_3O_4, FeOOH on the surface of the working electrode (Al-Mg alloy mesh). In adidtion these phases could be combined among them leading diferent structures and morphologies like "core-shell" structures. Zero valence iron (Fe^0) can be oxidized by oxygen and water to form Fe(II) and/or Fe(III) oxides. Moreover, in this study, the extremely oxidative operative conditions should facilitate the oxygen dissolution as a contamination of as-plated Fe^0.[21] This oxygen may react and oxidized Fe^{2+} to Fe^{3+} at the interface of the electrode producing non-soluble hematite (α-Fe_2O_3) through some iron hydroxide intermediates. The equations which explain the different reactions taken place in the formation of the iron phases are the following:

$$4\ Fe^{2+} + 3\ O_2 \rightarrow 2\ Fe_2O_3 \quad (1)$$
$$12\ Fe^{2+} + 3\ O_2 + 6\ H_2O \rightarrow 4\ Fe(OH)_3 \quad (2)$$
$$Fe(OH)_3 \rightarrow FeOOH + H_2O \quad (3)$$
$$2\ Fe(OH)_3 \rightarrow Fe_2O_3 + 2\ H_2O \quad (4)$$

On the other hand, Park *et al.* proposed a second reaction *via* hydrogen gas evolution and pH change favoring the formation of iron hydroxides which further condense with loss of water to magnetite or hematite because of their higher thermodynamic stability. This reaction is presented by the following equation:

$$3\ Fe(OH)_2 \rightarrow Fe_3O_4 + H_2\ (g) + 2\ H_2O \quad (5)$$

With the increase of temperature the oxygen diffusion is higher and its solubility decreases, as a consequence, more anaerobic conditions are produced favoring magnetite formation as it is predicted in equation (5). This hypothesis is confirmed by the observation of bubbles on the working electrode during the PED, and in addition, probably due also to hydrogen evolution of water (electrolysis) decomposition or carbon monoxide of FA decomposition by Fe^0. Furhtermore, these results are in agreement with other studies[22] which reported that for particle diameter from 10 to 100 nm a typical core–shell structure based on metallic iron core could be covered by an iron oxide shell. Electrochemically synthesized iron–based particles were used as a catalytic precursor for the growth of carbon nanostructures by chemical vapor deposition (CVD).

Surprisingly, it was found that under identical CVD conditions only the electrodeposited material at 50 ºC by using a plating bath containing $FeCl_2$ and $Fe(NO_3)_3$ salts and those prepared at RT by using $FeCl_3$ salt were catalytically active for the growth of nanocarbons with different morphologies and microstructures. The rest of the samples were catalytically inactive under similar conditions. SEM images for those samples showed poor activity on the carbon deposition (Fig. 4S).

Figure 5 shows the SEM images for a typical carbon–rich nanostructures grown on Al–Mg substrate. Figures 5a and 5b show a typical spherical shape of micron-size particles evidencing in most cases a "core-shell" structure. The external part was made by Fe-based catalyst and the inert part contains the carbonaceous material. From this morphology we can infer that during the chemical vapor deposition the reacting gases (acetylene and hydrogen) diffuse inside the porous catalyst and then carbon starts its nucleation and growth on the inner surface of the particles following a root–growth mechanism.[23] From the images is also possible observed the formation of highly oriented carbon nanofilaments conecting two regions of the catalyst. Figure 5c shows the HRTEM images corresponding to an Fe oxide particle before CVD with clear signs of an elevated porosity in its structure which support our hyphotesis about the growth mechanism. SEM images of carbon nanostructures grown with Fe-based catalyst synthezed in a $FeCl_3.6H_2O$ bath at room temperature and $Fe(NO_3)_3.9H_2O$ bath at 50 ºC are reported in Figure 4S.

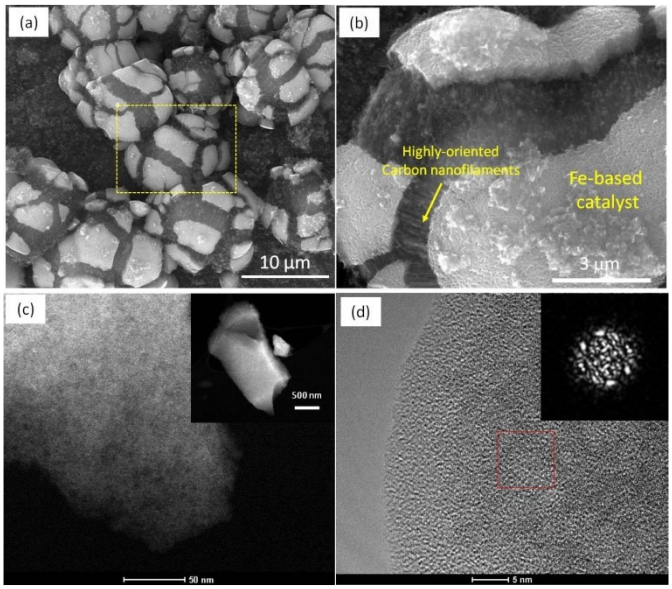

Fig. 5 SEM (a, b) images of carbon nanostructures grown on Al-Mg substrate and HRTEM (c,d) images of a porous catalyst iron-based structure before CVD for Fe-based catalyst synthesis in a $FeCl_2$ bath at 50 ºC.

In our recent report, we evidenced that an inter–diffusion of Mg, Fe, and O between the final electrodeposited Fe-based particles and the Al-Mg mesh generate flakes which become the active site for the nanocarbon growth[15]. Interestingly, the new results presented here show that there is a dependence on both the type of iron salt used during the plating process and the final composition of the iron oxide catalyst precursor (Table 2). Both iron oxide precursors, Fe_2O_3 and Fe_3O_4, were catalytically active for the synthesis of nanocarbons but under specific experimental bath conditions and temperature.

The oxidation state of the metal catalyst during the carbon nucleation has been under a controversial debate in the last years.[24,25] For instance, the study of Arcos *et al.*[26] shows that a dense growth of thin nanotubes are formed from metallic iron which transforms to Fe_2O_3 particles after annealing and evolves to FeO during the CVD. On the other hand, Teblum *et al.*[27] studied the correlation between the catalyst oxidation state and the growth behavior of aligned carbon nanotube forests by varying the thermal annealing conditions of an iron thin film catalyst. They reported that the catalytic activity increased in the following order: $Fe^0 > Fe_3O_4 > Fe_2O_3 > FeO$.

For the study of the carbon microstructure, again Raman spectroscopy has been used as a powerful analytical tool for this type of materials[27]. Figure 6 shows the Raman spectra of the carbon nanostructures grown on the Al-Mg mesh along with other carbonaceous materials and the pristine mesh as a comparative mode. Prominent peaks appear in the range of 1341-48 cm^{-1} (D, Disorder) and 1580-1605 cm^{-1} (G, Graphite). The G-band corresponds to the stretching of the C-C for sp^2 bonding of crystalline graphene sheets (E_{2g} mode), and the D-band is associated to defects or sp^3 bonding (A_{1g}, breathing mode).[29] The

relative intensity ratio of the D band and the G band, express as I_D/I_G, is known as an index to determine the degree of disorder of the carbon structure. In the aluminum alloy mesh treated under CVD conditions, there were no presence of carbon nanostructures neither signals corresponding to the D and G band. The rest of the as-deposited iron samples exhibit the same D and G band position than the carbon black but with a higher I_D/I_G ratio. Thus, the aromatic domains in the graphene sheet have a higher structural order or less defects content.

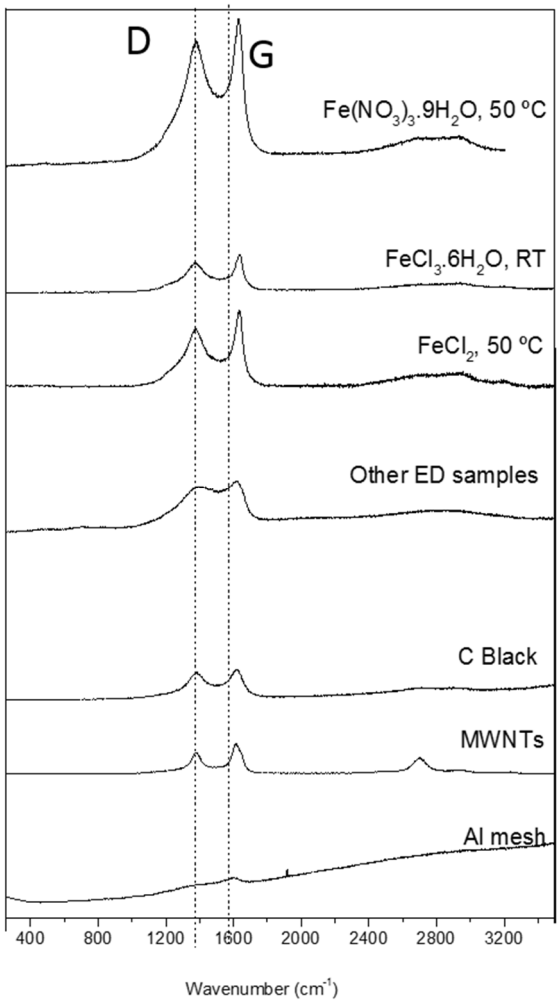

Fig. 6 Raman spectra of the susbtrate after CVD (a), MWCNT (b), carbon black (c), the samples treated without (d) and with carbon nanostructure growth: (e) 50 ºC, $FeCl_2$-based bath, (f) RT, $FeCl_3.6H_2O$-based bath and (g) 50ºC, $Fe(NO_3)_3.9H_2O$.

Table 1S indicates the positions of the D, and G band and their intensity ratio for the different carbonaceous materials. The carbon materials produced from the active iron catalysts precursors present a blue shift of the D band from 1341 to 1346 cm^{-1} while the G band is red shifted from 1601 to 1605 cm^{-1} with respect to carbon black. The downshift of G bands could also to some extent be assigned to the strained or curved graphite plane[28], while the upshift of the D band may be attributed as a charge transfer effect provided by chemical doping.[29]The sharp second order D peak (2710 cm^{-1}) observed in the Raman spectrum of multiwalled carbon nanotubes (MWCNTs) indicates the presence of small graphite clusters[30], which do not appear in the as–prepared samples. Furthermore, signals corresponding to iron phases were not observed. For this reason, we believe that during the CVD, the iron oxide deposited films may be reduce to metallic Fe or Fe_3C upon heating in H_2, both having Raman-inactive modes.

These results shown that the carbon nanostructures formed in Fig. 6 has a similar Raman feature than carbon black, though it exhibited bigger amount of defects and a more disorder structure. As a summary and to merge the different properties analized, Table 2 lists a summary of the PED conditions, chemical composition of the as–prepared iron–containing precursors, the success of synthesis of the grown of the nanocarbon structures, and I_D/I_G ratio. Not only a porous structure may help the formation of these carbon nanofilaments (Fig. 5), also the composition of catalyser as Fe_3O_4 phase is favored this reaction.

Table 2 Summary of the PED conditions, chemical composition of the as–prepared iron–containing precursors and the success of synthesis of the grown of the nanocarbon structures.

Salt	Bath temperature (ºC)	i_{max} (mA)	Composition	C structure grown	I_D/I_G
$FeCl_2$	RT	-0.05	α-Fe_2O_3	x	0.97
	50	-1.49	Fe_3O_4	✓	0.75
	100	-2.80	Fe_3O_4	x	0.97
$FeCl_3.6H_2O$	RT	-0.32	--	✓	0.78
	50	-1.52	Fe_3O_4	x	0.97
	100	-17.5	α-Fe_2O_3, Fe_3O_4	x	0.97
$Fe(NO_3)_3.9H_2O$	RT	-0.04	--	x	0.97
	50	-0.23	Fe_3O_4	✓	0.84
	100	-6.56	α-Fe_2O_3, Fe_3O_4	x	0.97

Experimental

Iron deposits were plated from solutions of iron salts in formamide (FA, Sigma-Aldrich) with a concentration of 0.3 M ($mol.L^{-1}$) and at different temperatures: room temperature (RT), 50 °C and 100 ºC. The iron source used were anhydrous $FeCl_2$ (Sigma-Aldrich), $FeCl_3.6H_2O$ (Sigma-Aldrich) and $Fe(NO_3)_3.9H_2O$ (Sigma Aldrich). Non aqueous system were chosen because of its chemical and air stability at room and higher temperature and its wide electrochemical window.

Linear sweep voltammetry (LSV) analysis was conducted to determine the potential reduction of oxidized iron species (Fe^{3+}, Fe^{2+}) to metallic iron at a scan rate of 0.5 $mV.s^{-1}$.

Pulsed electrochemical deposition (PED) was carried out in a conventional three electrode cell connected to a potentiostat/-galvanostat BioLogic VMP3. The working electrode was an aluminium-magnesium mesh (Alfa Aesar, purity about 99.7 %) with a surface area of 1.13 cm^2. Platinum foil (Goodfellow) with 6.2 cm^2 of surface area was employed as a counter electrode. The distance between the working and the platinum electrode was about 1.5 cm. The reference electrode was Ag/AgCl (Sigma–Aldrich). The work conditions were at -1.5 V *vs.* Ag/AgCl and 2000 pulses with a current–on time (T_{on}) of 0.001 s and a current–off time (T_{off}) of 0.01 s. These experiments were performed without stirring. After the electrochemical deposition the samples were rinsed with deionized water followed by ethanol. Afterwards, the samples were dried overnight under vacuum at 80°C and stored in a dessicator before using them during the chemical vapor deposition (CVD).

Carbon nanofilaments were prepared by chemical vapor deposition (CVD) by using the electrochemical deposited Fe material as catalyst precursor, from 20 sccm (standard cubic centimeters per minute) of acetylene (C_2H_2) gas diluted in a mixture of 70 v% of helium (He) as carrier gas, and 30 v% of hydrogen (H_2) at 525 °C to 575 °C, during 10 minutes.

The iron films deposited and the nanocarbons prepared by CVD were characterized by micro–Raman spectroscopy using a Renishaw *In Via* equipment equipped with a 532 nm diode laser. The total output power was of 0.3 mW, which was attenuated by a factor of 10 at the sample in order to avoid damage of the electrode surface. An objective with 50× magnification was used to focus the laser on the sample. The backscattered light was dispersed with a grating of 8000 lines/mm and detected on a multi–channel CCD detector.

The shape and morphology of the iron-based films were observed by SEM, TEM and HRTEM. SEM characterization was performed using a Quanta 200FEG and Quanta 250FEG SEMs operated at 30kV and equipped with an Apollo 10 SSD EDX detector. Transmission electron microscopy (TEM) and high-resolution transmission electron microscopy (HRTEM) experiments were carried out using a FEI Tecnai F20 G2 electron microscope operated at 200kV and Titan 60–300 with aberration correction operated at 80kV respectively. Both microscopes are equipped with High Angle Annular Dark Field (HAADF) detector and X-ray Dispersive Energy (EDX) spectrometer. Samples for TEM were dispersed in acetone, and transferred to a holey carbon film fixed on a 3 mm copper grid.

Conclusions

We have developed a methodology to growth carbon nanostructures in two steps, first, the synthesis of the catalyst *via* pulsed electrodeposition and second the carbon nucleation and growth by CVD. We were able to electrochemically synthesized crystalline phases of Fe_3O_4 and α-Fe_2O_3 in a non-aqueous solution of Fe^{2+} and Fe^{3+} based baths at room temperature and 50ºC without any thermal annealing previously to the electrodeposition. The morphology of the active catalyst precursors are composed of spherical nanoparticles with porous structure. From these results, we conclude that both the chemical composition and the structure of the catalyst are having crucial influence in the growth of carbon nanostructures. Then, carbon nanofilaments with a higher disorder degree (I_G/I_D = 0.87) than for carbon black materials (I_G/I_D = 0.75-0.84). These properties make them as a suitable material for the preparation of advanced electrodes in the energy storage field.

Acknowledgements

The authors gratefully acknowledge support by the Department of Industry, Innovation, Commerce & Tourism of the Basque Government through the Etortek Program. Prof. Michel Armand for his discussions and support.

Notes and references

[a] CIC EnergiGUNE, Alava Technology Park, Miñano, Álava, 01510, Spain

Electronic Supplementary Information (ESI) available: [details of any supplementary information available should be included here]. See DOI: 10.1039/b000000x/

1 a) AK. Geim, *Science* 2009, 324 (5934),1530. b) MFL. De Volder, SH. Tawfick, RH. Baughman, AJ. Hart, *Science*, 2013, 339(6119), 535.

2 RTK Baker. *Carbon* 1989, **27** (3), 315.

3 V. Avetik, R. Harutyunyan, G. Chen, T. M. Paronyan, E. M. Pigos, O.A. Kuznetsov, K. Hewaparakrama, S. Min Kim, D. Zakharov, E. A. Stach, G.U. Sumanasekera, *Science*, 2009, **326** (5949), 116-120.

4 Esconjauregui, S.; Whelan, C. M.; Maex, K. *Carbon* 2009 **47** 659-669.

5 Kumar, M. ; Ando, Y. *J. Nanosci. Nanotechnol*. 2010 **10** 3739–3758.

6 M.S. Chandrasekar, M. Pushpavanam, Electroch. Acta 2008 **53** 3313.

7 C.M. López, K.-S. Choi, *Langmuir* 2006 **22** 10625.

8 K.-S. Choi, *Dalton Trans.* 2008, **40** 5432.

9 C.S. Enache, Y.Q. Liang, R. van de Krol, *Thin Solid Films*, 2011, **520**,1034.

10 R.S. Schrebler, H. Altamirano, P. Grez, F. V. Herrera, E. C. Muñoz, L. A. Ballesteros, R. A. Córdova, H.Gómez, E. A. Dalchiele, *Thin Solid Films,* 2010 **518**, , 6844.

11 Y.L. Chueh, M.W. Lai, J.Q. Liang, L.J. Chou, Z.L. Wang, *Adv. Funct. Mater*., 2006 **16,** , 2243.

12 S. Chatman, A. J. G. Noel, K. M. Poduska, *J. Applied Phys*., 2005, **98**, 113902

13 T. A. Sorenson, S. A. Morton, G. D. Waddill, J. A. Switzer, *J. Am. Chem. Soc.,* 2002, **124**, 7604.

14 M. Cortes, E. Gomez, J. Sadler, E. Valles, *Electroch. Acta*, 2011, **56**, 4087.

15 J. Carretero-González, S Pérez-Villar, V.V.Roddatis, N.Gómez, O.B Bondarchuk, S Lopatin, C.M López, *Carbon,* 2014, **68,** 821

16 K.H. Choi et al. *J. Power Sources* 1998, **75,** 230.

17 B. Li, C. Fan, Y. Chen, J. Lou, L. Yan, *Electrochem. Acta*,2011, **56** 5478.

18 O. N. Shebanova, P. Lazor, *J. Solid State Chem.,* 2003, **174,** 424.

19 A. M. Jubb, H. C. Allen, *Appl. Mat. Interfaces* 2010, **2** (10), 2804

20 D.L.A. de Faria, S. Venancio Silva, M.T. de Oliveira, *J. Raman Spectrosc,.* 1997, **28,** 873.

21 *H. Park,* P. Ayala, M. A. Deshusses, A. Mulchandani, H. Choi, N. V. Myung, *Chemical Engineering Journal,* 2008, **139,** 208.

22 B. I. Kharisov, H. V. Rasika Dias, O. V. Kharissova, V. M. Jimenez Perez, B. Olvera Perez, B. Muñoz Flores, *RSC Advances,* 2012, **2,** 9325.

23 R. T. K Baker, J. R. Alonzo, J. A. Dumesic, D. J. C. Yates, *J. Catal.,* 1982, **77,** 74.

24 Baker, R. T. K.; Alonzo, J. R.; Dumesic, J. A.; Yates, D. J. C. J. Catal. 1982, 77, 74..

25 E. Teblum, Y. Gofer, C. L. Pint, G. D. Nessim, *J. Phys. Chem*. C, 2012, 116, 24522.

26 T. Arcos, M. Gunnar Garnier, J. Won Seo, P. Oelhafen,V. Thommen, D. Mathys, *J. Phys. Chem. B,* 2004, **108,** 7728.

27 F. Tuinstra, J.L. Koenig, *J. Chemical Physics,* 1970, **53,** 1126.

28 S. Reich, C. Thomsen, J. Maultzsch *Carbon nanotubes*. Berlin: Wiley; 2004. p. 135.

29 A. C. Ferrari, J. C. Meyer, V. Scardaci, C. Casiraghi, M. Lazzeri, F. Mauri, S. Piscanec, D. Jiang, K. S. Novoselov,4 S. Roth, A. K. Geim, *Spectroch. Acta Part A*, 2014, **121,** 715.

30 M. S. Dresselhaus, A. J. M. Hofmann, G. Dresselhaus, R. Saito, *Nano Lett,.* **10,** 2010, 751.